Rotation-induced nonlinear wavepackets in internal waves

A. J. Whitfield and E. R. Johnson

Citation: Physics of Fluids (1994-present) **26**, 056606 (2014); doi: 10.1063/1.4879075
View online: http://dx.doi.org/10.1063/1.4879075
View Table of Contents: http://scitation.aip.org/content/aip/journal/pof2/26/5?ver=pdfcov
Published by the AIP Publishing

PHYSICS OF FLUIDS **26**, 056606 (2014)

Rotation-induced nonlinear wavepackets in internal waves

A. J. Whitfield[a] and E. R. Johnson[b]
Department of Mathematics, University College London, London WC1E 6BT, United Kingdom

(Received 30 August 2013; accepted 10 May 2014; published online 28 May 2014)

The long time effect of weak rotation on an internal solitary wave is the decay into inertia-gravity waves and the eventual formation of a localised wavepacket. Here this initial value problem is considered within the context of the Ostrovsky, or the rotation-modified Korteweg-de Vries (KdV), equation and a numerical method for obtaining accurate wavepacket solutions is presented. The flow evolutions are described in the regimes of relatively-strong and relatively-weak rotational effects. When rotational effects are relatively strong a second-order soliton solution of the nonlinear Schrödinger equation accurately predicts the shape, and phase and group velocities of the numerically determined wavepackets. It is suggested that these solitons may form from a local Benjamin-Feir instability in the inertia-gravity wave-train radiated when a KdV solitary wave rapidly adjusts to the presence of strong rotation. When rotational effects are relatively weak the initial KdV solitary wave remains coherent longer, decaying only slowly due to weak radiation and modulational instability is no longer relevant. Wavepacket solutions in this regime appear to consist of a modulated KdV soliton wavetrain propagating on a slowly varying background of finite extent.
 [http://dx.doi.org/10.1063/1.4879075]

I. INTRODUCTION

Rotational effects are often regarded as negligible when describing the dynamics of internal solitary waves in the ocean, as the waves are short compared to the internal deformation radius of the stratified ocean. However, observed waves can persist for several days allowing rotational effects to become important. The main consequence of rotation is the decay of the otherwise persistent solitary wave into inertia-gravity waves that have been introduced into the system by rotation. Indeed this feature of rotational effects has received considerable attention recently. Simulations of various representative models, such as the Miyata-Choi-Camassa,[1] Ostrovsky,[2] Euler,[3] and regularised Boussinesq[4] equations, have all found that not only does rotation cause a solitary wave to decay but that for strong enough rotation a nonlinear wavepacket can eventually form from the original solitary wave radiation. These rotationally induced wavepackets have also been observed experimentally.[5]

The likelihood of whether the wavepackets could be observed under real oceanic conditions is currently under debate. While it is accepted that rotational effects on internal solitary waves are evident in locations of interest, such as the South China Sea[6,7] and the Strait of Gibraltar,[8] the time required for a nonlinear wavepacket to form, approximately several days at mid-latitude, suggests observing the packets might prove difficult. Simulations of the full rotating stratified Euler equations, which have probably produced the most representative study of purely rotational effects in real oceanic conditions, reported that for mid-latitudinal parameters, rotational effects were not strong enough for the nonlinear wavepackets to form.[3]

For oceanic internal solitary waves it is regularly assumed their amplitudes are small compared with the ocean depth (weak nonlinearity) and their wavelength is long compared with the ocean depth

[a]Electronic mail: ashley.whitfield.12@ucl.ac.uk
[b]Electronic mail: e.johnson@ucl.ac.uk

(weak dispersion). Based on these assumptions Korteweg-de Vries (KdV) theory is an appropriate approximation and the simplest model that takes into account the effects of rotation within this framework is the Ostrovsky (rotation-modified KdV) equation. The purpose of this study is to discuss the underlying phenomena of rotationally-induced wavepackets, on the assumption that any qualitative features present in an analysis of the Ostrovsky equation are likely to be present in the fully nonlinear set of equations.

Section II introduces the scaled Ostrovsky equation that forms the basis of the discussion here. It is noted that there are two distinct evolution regimes, of relatively strong and relatively weak rotational effects, depending on the amplitude of the initial disturbance to this scaled equation. Small initial scaled disturbances correspond to strong rotational effects, the problem is close to one of linear wave dispersion and the dynamics of the linear waves is paramount. In particular, the group velocity of the linear waves has a maximum at a finite non-zero wavenumber, $k_c = 3^{-1/4} \sim 0.76$. Analysis[2] in the neighbourhood of the wavenumber k_c has been the basis of the only theory to date to successfully predict any details of the wavepackets emerging in simulations. Technical difficulties arise since for wavenumbers k sufficiently close to k_c the usual nonlinear Schrödinger equation (NLS) analysis ceases to apply and a higher-order NLS theory is required for the packets.

A well-known mechanism for wavepacket formation[9,10] is modulational instability (MI), or, in the context of water waves, Benjamin-Feir instability: a nonlinear process by which a dominant harmonic carrier wave can interact with infinitesimal sidebands resulting in the exponential growth of the sideband frequencies. The oceanic KdV equation is not modulationally unstable, although modifications such as an additional cubic nonlinearity term, as in the extended KdV, can introduce MI.[11] The Ostrovsky equation has also been shown to be focussing at some wavenumbers[2] and so allow Benjamin-Feir instability. Thus Sec. III briefly notes the relevant results of the usual MI analysis, including the constraint on modulation wavenumber, and shows, through numerical simulations, that the results accurately describe the instabilities seen in both wavetrains and Gaussian packets for $k = 0.80$ and $k = 0.90$. The significance of these simulations arises from noting that the wavenumbers observed in the subsequent, numerically-determined wavepacket solutions of the Ostrovsky equation all lie above $k = 0.80$ and so lie in a parameter range where the usual MI appears to be valid.

Section IV discusses the evolution of an initial KdV soliton in the Ostrovsky equation. In the strong-rotation, small-amplitude, near-linear regime, a local criterion for Benjamin-Feir instability of the dispersing inertial-gravity wave train is introduced which predicts that a wavepacket should form slightly behind the leading linear waves and should travel more slowly. This is confirmed by comparison of an Ostrovsky equation simulation with a purely linear computation. The shape and phase and group speeds of these wavepackets are shown to be accurately predicted by the usual NLS soliton, particularly when second-order (in amplitude) terms are included, and simulations indicate that these NLS solitons are persistent solutions of the equations. The simulations show that for these packets higher-order (in $(k - k_c)$) dispersion is only a small perturbation, leading to the formation of exponentially small tails.[12,13] In the weak-rotation, large-amplitude, near-KdV regime the MI mechanism of packet formation is not relevant. The small-time behaviour in this regime consists of a propagating KdV soliton decaying slowly due to weak inertia-gravity wave radiation.[2,14] Wavepacket solutions in this regime no longer resemble NLS solitons but are shown to more closely resemble a KdV soliton wavetrain propagating on a slowly varying background of finite extent. Section V gives a brief discussion.

II. THE OSTROVSKY EQUATION

The KdV equation for internal solitary waves expressed in a reference frame moving at linear long wave speed is

$$\eta_t + \nu\eta\eta_x + \beta\eta_{xxx} = 0, \tag{1}$$

where η represents the interfacial displacement, ν is the strength of weak nonlinearity, and β is weak hydrostatic dispersion (see Ref. 5 for more details). The KdV equation is fully integrable via the inverse scattering transform,[15] from which exact solitary wave solutions can be obtained. The

Ostrovsky equation

$$(\eta_t + \nu\eta\eta_x + \beta\eta_{xxx})_x = \gamma\eta \tag{2}$$

is a linear long-wave perturbation to the KdV equation, where γ is a measure of the strength of weak rotation. A consequence of adding the linear long-wave term to the right-hand side of the KdV equation is to remove the spectral gap required for the existence of solitary wave solutions and hence (2) predicts the destruction of the KdV solitary wave due to rotation.[14,16]

The Ostrovsky equation is inherently a weakly nonlinear model leading to its being inaccurate in the small and large wavenumber limits. Past comparisons with the full Euler equations have shown a quick divergence of quantitative results[17] and it has been hypothesised that this is a result of an unphysical unbounded frequency in the Ostrovsky equation.[3] Despite this, for the problem of the decay of a solitary wave considered here all models appear in agreement that for sufficiently strong rotation a solitary wave decays and a nonlinear wavepacket emerges.

For the case of oceanic internal solitary waves it can be assumed without loss of generality that $\nu\beta > 0$ and $\gamma > 0$. Therefore, it is sufficient to consider the dimensionless Ostrovsky equation,

$$(\tilde{\eta}_t + \tilde{\eta}\tilde{\eta}_x + \tilde{\eta}_{xxx})_x = \tilde{\eta}, \tag{3}$$

obtained[2] by introducing

$$x = L\tilde{x},\ t = T\tilde{t},\ \eta = M\tilde{\eta} \quad \text{with} \quad L^4 = \beta/\gamma,\ T = L^3/\beta,\ M = \beta/\nu L^2. \tag{4}$$

Equation (3) with "tildes" dropped will henceforth be referred to as the Ostrovsky equation. Although Eq. (3) is parameter free, the initial condition for any flow evolution introduces two scales: the length scale and the amplitude of the initial η. An initial condition of amplitude A can be re-scaled to unity by scaling η on A, x on $A^{-1/2}$, and t on $A^{-3/2}$, giving once again Eq. (3) with however a factor of A^{-2} multiplying the right side. The spatial scaling is the standard KdV scaling and is satisfied by the KdV soliton initial conditions considered in Sec. IV. Thus small amplitude initial conditions ($A \ll 1$) correspond to strong rotational effects, with the initial dynamics close to linear and dominated by rapid formation of a linear wavetrain from any initial disturbance. Large amplitude initial conditions ($\epsilon = A^{-1} \ll 1$) correspond to weak rotational effects, with the initial dynamics close to KdV dynamics and an initial KdV soliton decaying only slowly due to weak linear wave radiation.[14,16] The parameter ϵ here corresponds precisely to ϵ in Ref. 18. For ease of comparison with earlier work, results are described in Sec. IV in terms of the amplitude of the initial conditions however, because of this scaling, the large amplitude solutions should be regarded as weak-rotation near-KdV wavepackets of order unity amplitude and thus remain well within the validity of the Ostrovsky equation.

The dispersion relation, phase, and group velocity of linear waves in the Ostrovsky equation are

$$\omega_0 = 1/k - k^3, \quad c_p = -k^2 + 1/k^2 \quad \text{and} \quad c_g = -3k^2 - 1/k^2, \tag{5}$$

for wavenumber k. The linear group velocity, with maximum $c_g(k_c)$ at $k_c = 3^{-1/4}$, is shown in Fig. 1(a). In describing rotationally-induced nonlinear wavepackets, this maximum $c_g(k_c)$ has been a subject of interest, as previous studies[1,2] have described packets as propagating with the fastest group velocity of all the emitted radiation. This has posed a technical difficulty in the analysis as the second-order dispersion, $\omega_{0kk} = \mathrm{d}^2\omega_0/\mathrm{d}k^2$ (see Fig. 1(b)), is zero at $k = k_c$ and so describing the wavepacket modulation through nonlinear Schrödinger theory becomes more complicated.[2]

III. BENJAMIN-FEIR INSTABILITY

A. Background

A fundamental result of MI analysis[19] is that weakly nonlinear waves with an amplitude-dependent dispersion relation

$$\omega = \omega_0(k) + \omega_2(k)a^2 + \mathcal{O}(a^4) \tag{6}$$

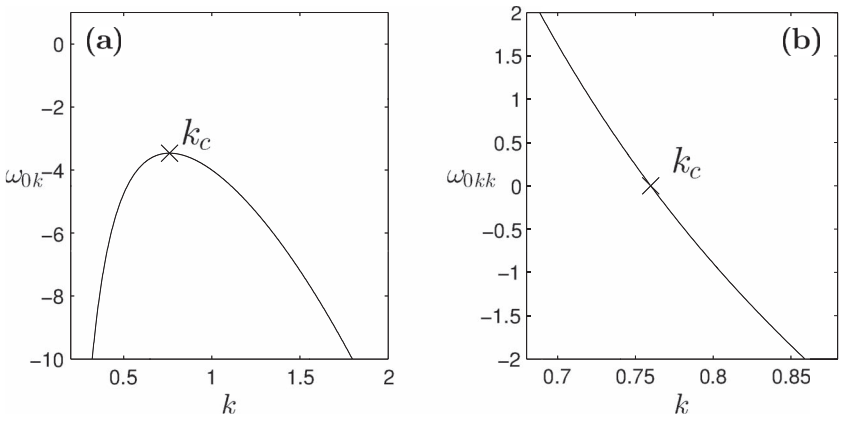

FIG. 1. (a) The linear group velocity c_g ($\mathrm{d}\omega_0/\mathrm{d}k = \omega_{0k}$) and (b) the second-order dispersion ω_{0kk}, for the Ostrovsky equation as a function of the wavenumber k showing the critical wavenumber k_c.

(where a is a measure of the amplitude, ω is the frequency, and ω_2 is a nonlinear correction to the linear dispersion relation ω_0), are Benjamin-Feir unstable if the Benjamin-Feir-Lighthill (BFL) criterion

$$\omega_{0kk}\omega_2 < 0 \tag{7}$$

holds for some k. The sign of nonlinear correction in (6) determines the stability of the wave train. One approach to obtaining the ω_2 term is a weakly nonlinear theory developed for water waves by Hasimoto and Ono.[20] This requires deriving a NLS for the Ostrovsky equation that to leading order describes the modulation of the wave groups.

Grimshaw and Helfrich first derived the NLS for the Ostrovsky equation by the derivative expansion method.[2] Their asymptotic analysis was based on the assumption of small amplitude (weak nonlinearity) in the Ostrovsky equation and an asymptotic expansion of the form

$$\eta(x,t) = A_o + A\exp(\mathrm{i}\theta) + \text{c.c.} + \mathrm{A}_2\exp(2\mathrm{i}\theta) + \text{c.c.} + \ldots, \tag{8}$$

where c.c. denotes the complex conjugate of the preceding term, $\theta = kx - \omega t$ and $|A| \ll 1$. It is assumed in the above expansion $A(x, t)$ is slowly varying and $A_2 \sim \mathcal{O}(|A|^2)$. These assumptions are sufficient to show[2] that $A_0 \sim \mathcal{O}(|A|^4)$ and the leading order term A satisfies the NLS,

$$\mathrm{i}A_t + \tfrac{1}{2}\omega_{0kk}A_{XX} - \omega_2|A|^2A = 0, \tag{9}$$

with $\omega_2(k) = 2k^3/(12k^4 + 3)$ and $X = x - c_g t$.

An exact solution of the NLS is given by

$$A = a\exp(-\mathrm{i}\omega_2 a^2 t), \tag{10}$$

which corresponds in the original problem to the asymptotically correct solution,

$$\eta \approx 2a\cos(kx - (\omega_0 + \omega_2 a^2)t), \tag{11}$$

i.e., a plane wave with a small frequency shift resulting from nonlinearity. Note expansion (8) requires $|A| \ll 1$, so for (11) to be valid $a \ll 1$ and hence a has taken the role here of a small parameter. Since $\omega_2 > 0$ for all k, the sign of the BFL criterion is determined by ω_{0kk}. Now ω_{0kk} is positive for $k < k_c$ and negative for $k > k_c$ and so a small amplitude plane wave solution of the Ostrovsky equation is stable when $k < k_c$ and unstable when $k > k_c$. In the absence of rotation, the Ostrovsky equation reduces to the KdV equation for which $\omega_2 > 0$ for all k also but $\omega_{0kk} > 0$ for all k and so the KdV equation is modulationally stable.[11] Rotation thus introduces modulational or Benjamin-Feir instability.[2]

Solution (11) corresponds to the original water-wave problem considered by Benjamin and Feir,[21] and the details of the instability are well understood. For a slight modulation of the form

$$\eta = 2a(1+\delta)\cos(kx - (\omega_0 + \omega_2 a^2)t), \tag{12}$$

where $|\delta(Kx, t)| \ll 1$ is a function of x and t of typical wavenumber K, linear stability analysis confirms that when the BFL criterion is satisfied, (12) is unstable to modulations δ, provided K satisfies

$$0 < K < K_c \quad \text{where} \quad K_c = a\,(-4\omega_2/\omega_{0kk})^{1/2}\,, \tag{13}$$

and the growth rate of the modulation δ is

$$\Gamma = (K/2)|\omega_{0kk}|\sqrt{K_c^2 - K^2}. \tag{14}$$

Now Γ is accurate for $e^{\Gamma t} \ll 1$. At longer times the decrease in the initial carrier wave amplitude a must be taken into account and this results in the eventual reversal of the process, i.e., demodulation. The repeating cycle of increased modulation then demodulation is termed recurrence.[22] Two conditions must thus be met for MI: the BFL carrier wavenumber condition (7) and the modulation wavelength and amplitude condition (13).

B. Numerical simulations

The results noted above, valid in the small amplitude ($A \ll 1$), strong rotation ($\epsilon = A^{-1} \gg 1$) regime, are examined here in a series of numerical simulations of the Ostrovsky equation (3) using the method of integrating factors[23] with a pseudo-spectral method on a periodic domain in x and 4th order Runge-Kutta Cash-Karp[24] adaptive time-stepping in t with the error controlled in Fourier space. The initial conditions are taken as modulated plane wave solutions (11), of the form

$$\eta(x, 0) = 2a(1 + \delta(Kx))\cos(kx), \tag{15}$$

for the three cases

$$\delta(Kx) = 0, \quad \delta(Kx) = 0.1\sin(Kx), \quad \delta(Kx) = \exp(-K^2x^2) - 1, \tag{16}$$

i.e., an unmodulated plane wave, a periodic sinusoidal modulation, and a localised Gaussian modulation. To remain within the validity of small amplitude theory, the simulations take $a = 0.1$.

Fig. 2 shows the simulation of a plane wave with wavenumber $k = 0.80$, 5% larger than k_c, and no modulation, i.e., $\delta(Kx) = 0$. At sufficiently large time the plane wave has become modulationally unstable, due to the growth of numerical noise, showing that Benjamin-Feir instability exists in the Ostrovsky equation even close to k_c. Although not shown, the simulation of a plane wave with $k < k_c$ remained stable for all time.

Now consider restriction (13) on the wavenumber K of the envelope δ. The run times in the following simulations have been chosen so that an initially stable modulation does not have sufficient time to demodulate to the point that it becomes unstable due to recurrence. Fig. 3 shows results

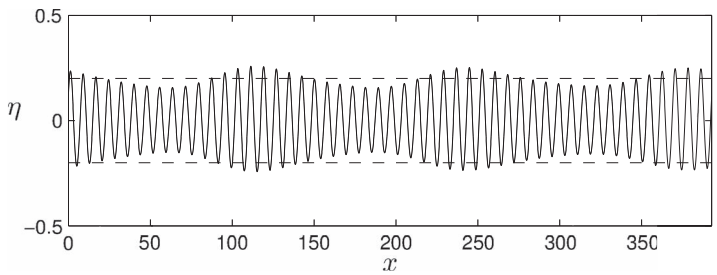

FIG. 2. An unstable plane wave of height $2a = 0.2$ at $t = 26\,000$ testing the BFL criterion where BFL <0 ($k = 0.8 > k_c$). The dashed lines in the figure show the modulation envelope at $t = 0$. The instability is due to the exponential growth of numerical noise.

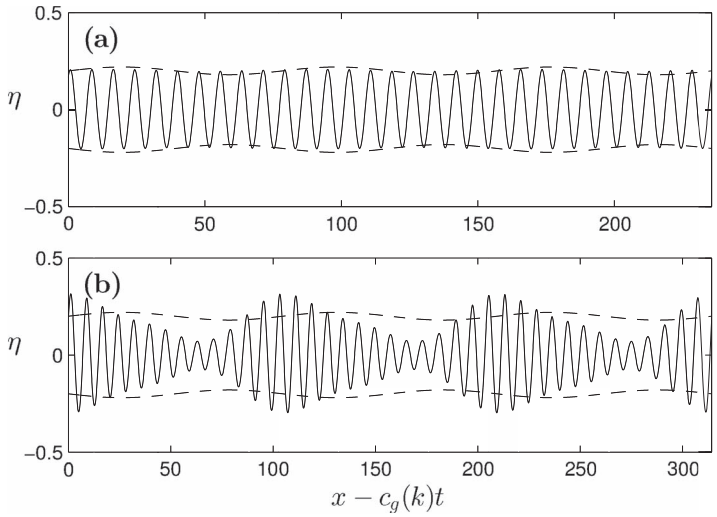

FIG. 3. Plane waves of height $2a = 0.2$ satisfying the BFL criterion for instability ($k = 0.8$) with sinusoidal modulations of different wavelengths K shown relative to a frame moving at the group velocity of the carrier wave. (a) Stable modulation at $t = 2000$ with $K > K_c$ ($K = 0.08$). (b) Unstable modulation at $t = 2000$ with $K < K_c$ ($K = 0.06$). The dashed lines in both figures show the modulation envelope at $t = 0$.

of a plane wave simulation with carrier wavenumber $k = 0.80$ and periodic sinusoidal modulation $\delta(Kx) = 0.1\sin(Kx)$. For the case of the stable modulation $K > K_c$ (Fig. 3(a)), a slight demodulation can be seen from the initial condition. This is best demonstrated by noting that the height of the peaks in the final form of the modulation is less than the original. For the modulation with $K < K_c$ (Fig. 3(b)) it is clear the disturbance grows as expected. Additional simulations of the periodic sinusoidal modulation, not shown in Fig. 3 were all in exact agreement with criterion (13), showing that (13) needs to be satisfied in addition to (7) for instability to occur and that these criteria are accurate for k within 5% of k_c.

Finally, as a basis for the discussion in Sec. IV, a localised Gaussian modulation, $\delta(Kx) = \exp(-K^2x^2) - 1$, is considered. Here the condition $\delta \ll 1$ does not hold and there is no envelope wavenumber in the traditional sense with K serving only as a characteristic inverse length scale. The stability theory for modulation states that there is a critical envelope wavenumber K_c such that all K below K_c are unstable and all K above K_c are stable. Thus it is to be expected that for sufficiently large K the localised structure will obey the linear theory of dispersive waves and the structure will disperse away, and for sufficiently small K the modulation will increase due to instability. To test this hypotheses K_c is approximated as 0.0225, where $2a$ has been taken in (13) to be the half height of the localised structure, and K's are chosen such that they are sufficiently far away from the approximate critical envelope wavenumber K_c. Fig. 4 shows that the Gaussian modulation for large K (Fig. 4(a)) disperses, whereas the modulation with small K (Fig. 4(b)) grows.

IV. WAVEPACKET EMERGENCE

A. Linear (strong rotation) evolution

Section III illustrated the Benjamin-Feir instability of the small-amplitude ($A \ll 1$), strong-rotation ($\epsilon = A^{-1} \gg 1$), near-linear regime of the Ostrovsky equation. It is now hypothesised that in this regime, this instability could be the mechanism of creation for the rotationally-induced nonlinear wavepackets that have been observed to evolve from the decay of an internal solitary wave due to rotation. The proposed mechanism is that strong rotation causes an initial disturbance to rapidly disperse into a long linear wavetrain where the amplitude and phase (and so wavenumber) of the linear wavetrain is a slowly varying function of position. This linear wavetrain is initially stable to Benjamin-Feir instability but evolves to become unstable, selecting a particular position for

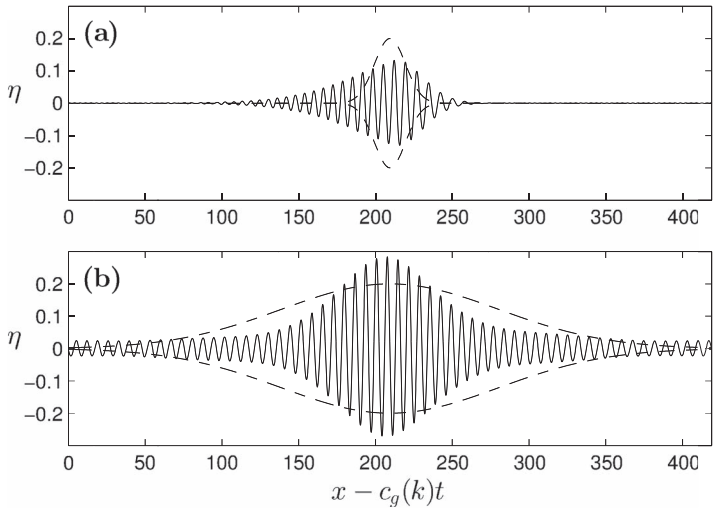

FIG. 4. Plane waves of height $2a = 0.2$ satisfying the BFL criterion for instability ($k = 0.9$) with localised Gaussian modulations of different wavelengths K shown relative to a frame moving at the group velocity of the carrier wave. (a) A stable modulation at $t = 100$ with large K ($K = 0.07$) has spread through linear dispersion. (b) An unstable modulation at $t = 1500$ with small K ($K = 0.01$) has grown. The dashed lines in both figures show the modulation envelope at $t = 0$.

the growth of a nonlinear wavepacket and thus also a particular wavenumber (and hence also group and phase speed).

The initial conditions are taken to be those of Ref. 2, i.e.,

$$\eta(x, 0) = a_s \mathrm{sech}^2 (x/D) \quad \text{where} \quad D^2 = 12/a_s, \tag{17}$$

the exact solitary wave solution of the KdV equation when the effects of rotation are not present (Fig. 5(a)). The solution of the linear Ostrovsky equation can be expressed as an inverse Fourier transform,

$$\eta(x, t) = \frac{1}{2\pi} \int_{-\infty}^{\infty} \hat{\eta}_0(k) \exp[\mathrm{i}kx - \mathrm{i}\omega_0(k)t] \, \mathrm{d}k, \tag{18}$$

where $\omega_0(k)$ is given by the linear dispersion relation and

$$\hat{\eta}_0(k) = \int_{-\infty}^{\infty} \eta(x, 0) \exp(\mathrm{i}kx) \, \mathrm{d}x = a_s k\pi D^2 \mathrm{cosech}\,(k\pi D/2)\,, \tag{19}$$

is the Fourier transform of the KdV solitary wave initial condition.

A preliminary simulation of the solitary wave decay using the initial condition from (17) with $a_s = 3$ is shown in Fig. 5. Each panel shows the linear solution (upper plot) obtained from a direct inversion of (18) using at least 10^6 grid points on a domain of length exceeding 10^5 and (lower plot) the full numerical nonlinear solution of the initial value problem. Fig. 5(b) shows that, for this small amplitude, even by $t = 500$ there is little difference between the linear and nonlinear solutions, suggesting that the numerical integration method is accurate and that consideration of the linear dispersive wave problem for these times is useful. Closer inspection of Fig. 5(b) shows that the only noticeable difference is what appears to be a slight amplitude growth for the waves between the first two linear "humps." The next time evolution, $t = 1000$ (Fig. 5(c)), shows a further increase in amplitude for the wave groups located at the same point in the wavetrain. This nonlinear growth can be seen continuing until $t = 2500$ (Fig. 5(f)) where it appears a wavepacket is forming. Similarities with the simulations in Sec. III suggest that this growth might be related to Benjamin-Feir instability in the dispersing wavetrain. The dashed line in the panels of Fig. 5 shows the location of the maximum linear group velocity $c_g(k_c)$ that previous studies[1,2] have suggested as the wavepacket speed. The growth or instability and hence the wavepacket appears to be located slightly to the left of this suggesting that the wavenumber of the packet in this simulation might differ from k_c.

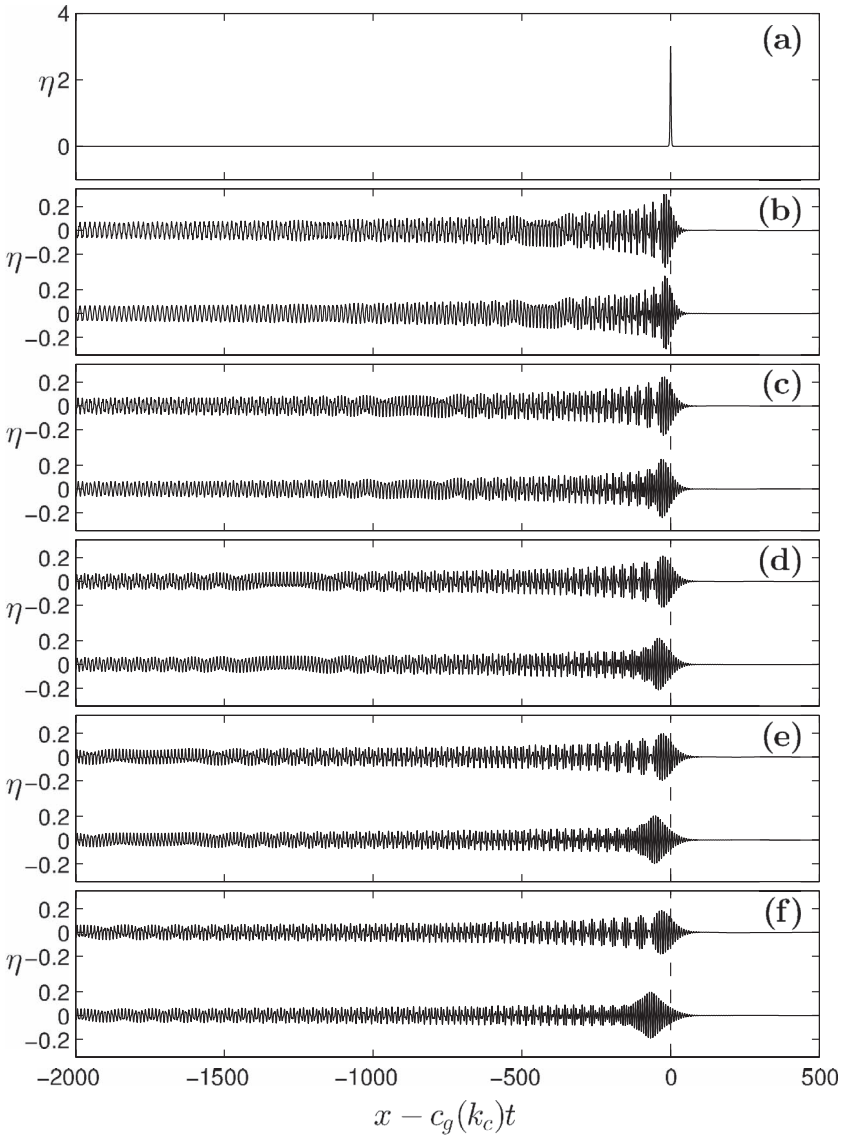

FIG. 5. The time evolution of the linear (upper) and full nonlinear (lower) Ostrovsky equation shown relative to a frame moving at the maximum linear group velocity, $c_g(k_c)$ for a KdV soliton of amplitude $a_s = 3$. (a) The initial condition, (b) $t = 500$, (c) $t = 1000$, (d) $t = 1500$, (e) $t = 2000$, and (f) $t = 2500$. The dashed line in (b)–(f) corresponds to a point initially at the origin and moving at $c_g(k_c)$ and so is fixed in this frame. Note the nonlinear growth located to the left of $c_g(k_c)$.

By $t = 500$ (Fig. 5(b)), the linear solution has dispersed sufficiently to be accurately described using the method of stationary phase (MSP).[25] For wavenumbers away from k_c, this gives the leading order behaviour of (18) as the sum of two slowly varying linear wavetrains,

$$\eta(x,t) \approx \eta_+ + \eta_-, \quad t \to \infty, \tag{20}$$

where

$$\eta_+ = 2A_+\cos(k_+x - \omega_0(k_+)t + \pi/4), \tag{21a}$$

$$\eta_- = 2A_-\cos(k_-x - \omega_0(k_-)t - \pi/4), \tag{21b}$$

with

$$A_+ = \hat{\eta}_0(k_+)[2\pi|c_g'(k_+)|t]^{-1/2}, \quad A_- = \hat{\eta}_0(k_-)[2\pi|c_g'(k_-)|t]^{-1/2}, \tag{22}$$

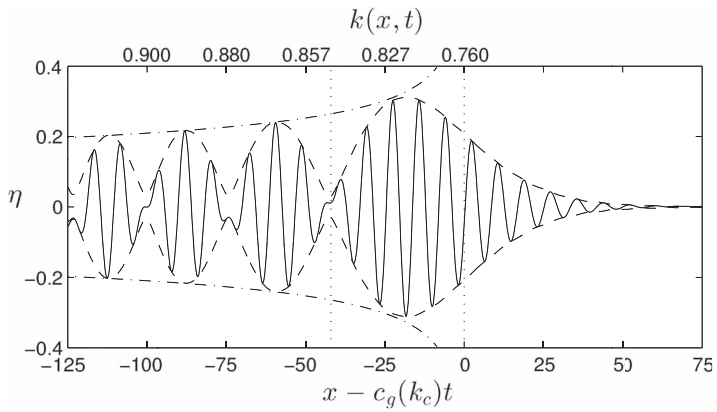

FIG. 6. A comparison at $t = 500$ of the two-phase stationary phase approximation (dashed-dotted lines) with the full linear solution (solid line) of the Ostrovsky equation for an initial solitary wave of amplitude $a_s = 3$ relative to a frame moving at the linear group velocity $c_g(k_c)$. The envelope of the linear solution (dashed lines) was obtained by the usual Hilbert transform method. The vertical dotted lines show the measured k value for the wavepacket that eventually forms (left line) and k_c (right line).

and

$$k_{\pm}(x,t) = 6^{-1/2}\left\{-(x/t) \pm \left[(x/t)^2 - 12\right]^{1/2}\right\}^{1/2}. \tag{23}$$

The two-phase approximation (20) explains the amplitude-modulated structure that appears, strongly in the linear solution and slightly less markedly in the nonlinear solution, behind the leading packet at times $t > 500$. Close behind the leading packet of the wavetrain, η_+ and η_- have approximately the same amplitude, and wavenumbers k_+ and k_- lying approximately equidistantly above and below k_c. The combined wave (20) is thus a beat pattern with order unity modulation and carrier frequency k_c. Closer to the wavefront, for $x \to c_g(k_c)t$, the stationary points $k_\pm$ coalesce at k_c, giving a single packet which decays more slowly with time ($t^{-1/3}$ versus $t^{-1/2}$), an Airy function envelope with carrier frequency k_c. This is noticeable in Fig. 5(b) where the linear wavetrain is largest near the origin. The small difference between the linear and nonlinear wavetrains at $t = 500$ means that estimates of wavepacket speed at times $t < 500$ would return the linear value of $c_g(k_c)$ (as would measurement for $t < 100$ for $a_s = 4$ in Fig. 8), perhaps related to the wavepacket speeds for small a_s reported in Ref. 2. Fig. 6 shows that the position where the wavepacket appears to begin growing (between the first two linear humps) coincides with the wavenumber of the nonlinear wavepackets that eventually emerge in the long-time full numerical simulations (reported below) and that both lie to the left of the region of coalescence so that the two-phase approximation gives an adequate description of the wavetrain at the time and position of emergence.

Equation (20) gives an expression for a slowly varying wavetrain. Three significant differences between the slightly-modulated plane wave results noted in Sec. III and (20) are that the wavetrain consists of the superposition of two linear waves (21a), that the components $\eta_\pm$ have non-constant local wavenumbers $k_\pm(x, t)$ and that, similar to the localised Gaussian modulation example, there is no explicit envelope wavenumber as the modulation is non-periodic. To apply the results of Sec. III, we suppose that the two linear wavetrains can be treated separately, that $\eta_\pm$ vary sufficiently slowly that the local wavenumbers $k_\pm$ and modulation amplitude A_+ can be taken as constant, and that the wavenumber of the envelope η_+ can be estimated as

$$K \sim \frac{1}{A_+}\frac{\mathrm{d}A_+}{\mathrm{d}x}. \tag{24}$$

Then, since $k_-(x, t) < k_c$, the wavetrain η_- is stable to MI according to the BFL criterion (7) but, since $k_+(x, t) > k_c$, the wavetrain η_+ is a candidate for MI and will be unstable if it locally also

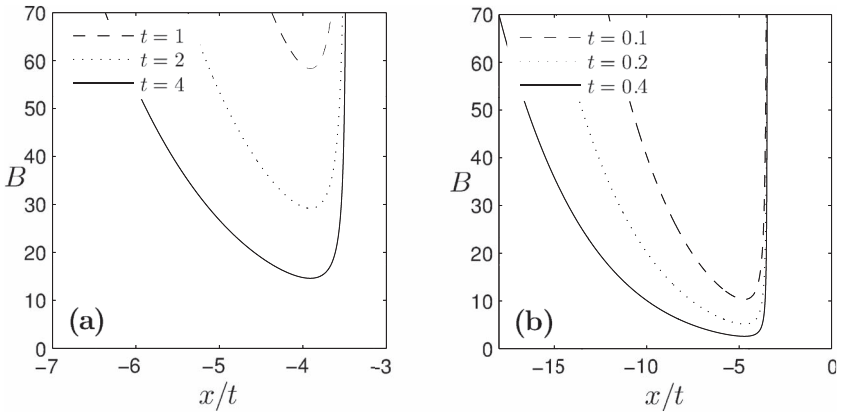

FIG. 7. The instability index $B(x, t)$ from (25) at various times for two different initial amplitudes a_s. (a) $a_s = 3$. (b) $a_s = 10$. Note the larger times required in (a) for B to fall to any particular value when compared to (b), implying that instability occurs at larger t for smaller initial amplitude solitary waves.

satisfies the modulation criterion (13) which becomes

$$B(x,t) < 4 \quad \text{where} \quad B(x,t) = -\frac{1}{A_+^4}\left(\frac{\mathrm{d}A_+}{\mathrm{d}x}\right)^2 \frac{\omega_{kk}}{\omega_2}. \tag{25}$$

If criterion (25) is satisfied at a point (x, t), then η_+ should be unstable at this point, although the approximations required to derive (25) mean that the estimate is not sharp.

Figs. 7(a) and 7(b) show plots at various times of $B(x, t)$ for initial solitary waves of amplitude $a_s = 3, 10$. The plots show that B has a single minimum in x/t and this minimum decreases monotonically in time, a property found for all a_s. As B decreases with time the minimum will be the first point to cross the threshold for MI ($B \sim 4$). Until then the wavetrain is locally stable and afterwards it is locally unstable. It is suggested that this is where weak nonlinear effects cause a wavepacket to grow in the linear wavetrain. The crossing point fixes the time t and position x where the wavepacket starts to grow and, through (23), the carrier wavenumber, k_B, of the wavepacket. The predicted carrier wavenumber k_B is compared to the numerically determined value below. As with the position where the wavepacket appears to begin growing and the wavenumber of the nonlinear wavepackets that eventually emerge, the point where the wavetrain η_+ first satisfies (25) lies within the region of validity of the two-phase stationary phase approximation. To decrease to the threshold $B \sim 4$, the evolution for $a_s = 3$ requires almost 40 times longer than that for $a_s = 10$. For all examples, smaller a_s take longer to reach the threshold and therefore it is to be expected that for smaller a_s instability occurs at larger t, and so smaller solitary waves should take longer to form a wavepacket, a result also obtained in Ref. 2.

B. Numerical simulations

The predictions of Sec. IV A are examined here by numerically integrating the Ostrovsky equation to follow the decay of an internal solitary wave (17) using the same numerical method outlined in Sec. III with, however, a sponge region added at each end of the periodic domain to absorb any radiation and so model computation on the physically relevant infinite domain. Previous numerical studies[2] have discussed extensively the evolution of the internal solitary wave to a nonlinear wavepacket and so here only a single example for a solitary wave with $a_s = 4$ (Fig. 8) is shown. In agreement with Ref. 2, Fig. 8(b) shows the eventual formation of a nonlinear wavepacket from the emitted radiation. Similar to Fig. 5, the packet appears to be a consequence of nonlinear growth to the left of the wave group at k_c (the dashed line in Fig. 8). The final time in the comparable evolution in Ref. 2 corresponds to $t = 100$ when the linear solution of Fig. 8(a) appears to differ little from the nonlinear solution of Fig. 8(b). Packet solutions arising from integrations initialised with KdV solitons of amplitudes $a_s = 3$, 10, and 80 are shown in Figs. 9(a)–9(c). These were obtained by integrating for a time sufficiently long that all linear radiation had separated totally from the packet.

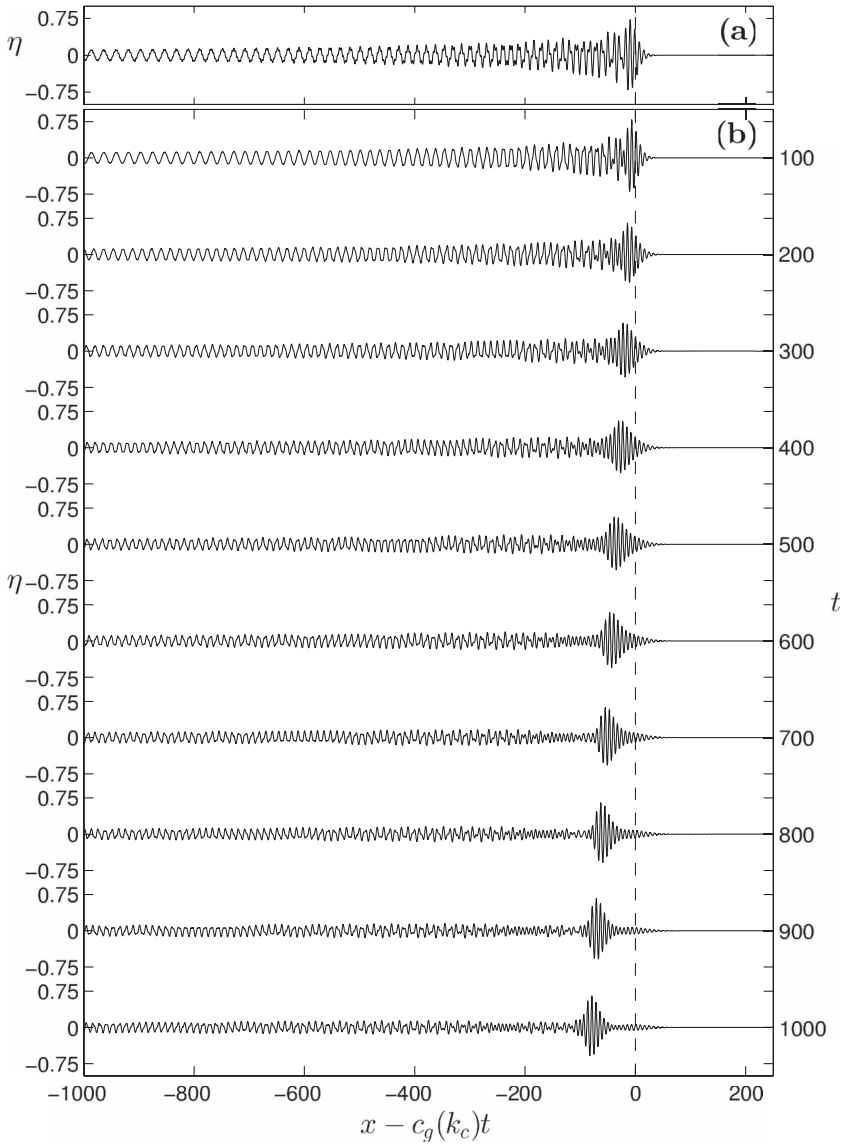

FIG. 8. Packet emergence for an initial amplitude of $a_s = 4$ in a frame moving with the linear group velocity $c_g(k_c)$. (a) The linear solution at $t = 100$. (b) The full Ostrovsky equation showing the evolution into a nonlinear wavepacket between times $t = 100$–1000. Note the similarity of the linear (a) and nonlinear (b) solutions at $t = 100$.

The integration was then continued and the packet group velocity s and period T of the packet obtained by considering the minimum of the function,

$$F(s, T) = \int_0^L (\eta(x, 0) - \eta(x - sT))^2 \, \mathrm{d}x \Big/ \int_0^L \eta^2(x, 0) \, \mathrm{d}x, \tag{26}$$

for L the length of the computational domain. The first minimum of F in the positive quadrant of (s, T) space estimates s and T and the minimum of F measures how close the solution is to periodic in the translating frame, being less than 10^{-5} for all converged packets discussed here. Once s and T are known other properties of a packet follow straightforwardly by considering the packet in the co-moving $x - st$ frame. Additional solutions (e.g., that of Fig. 9(d)), referred to here as *extended* packets, were generated using a scaled packet solution of lower amplitude as an initial profile for the evolution. Although packet solutions of the Ostrovsky equation, it appears that these extended packets are not accessible from initial conditions consisting of a simple isolated hump.

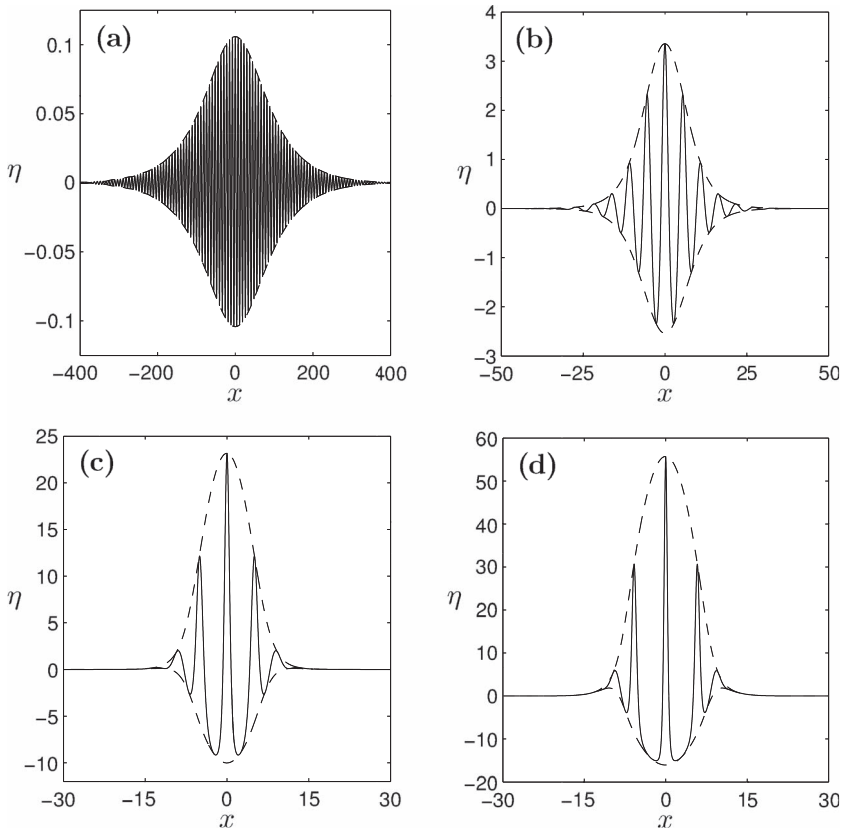

FIG. 9. Wave packet solutions of the Ostrovsky equation (solid lines) and their envelopes (dashed lines) created by solitary wave decay (a) $a_s = 3$, (b) $a_s = 10$, (c) $a_s = 80$, and (d) a higher, extended packet initialised using a scaled packet of lower amplitude.

The packet maximum and minimum values for solitary wave decay are shown in Fig. 10 as a function of initial amplitude a_s. There is a clear asymmetry in packet maximum and minimum for large a_s (weak rotation), and a peak in packet maximum appears at $a_s = 80$, after which increasing a_s has negligible effect on the final packet height, as all initial KdV solitons with $a_s \gtrsim 100$ evolve to the same packet. The packet asymmetry was observed in Ref. 2 as was the large a_s behaviour of

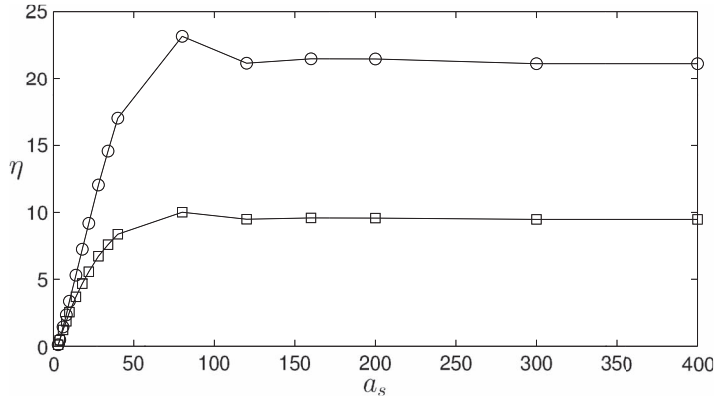

FIG. 10. The magnitudes of the packet maximum $\eta_{\max} = \max\{\eta(x,t)\}$ (circles) and minimum $\eta_{\min} = |\min\{\eta(x,t)\}|$ (squares) as a function of initial solitary wave amplitude a_s. For $a_s \gtrsim 100$, all initial solitary waves appear to evolve to the same packet solution.

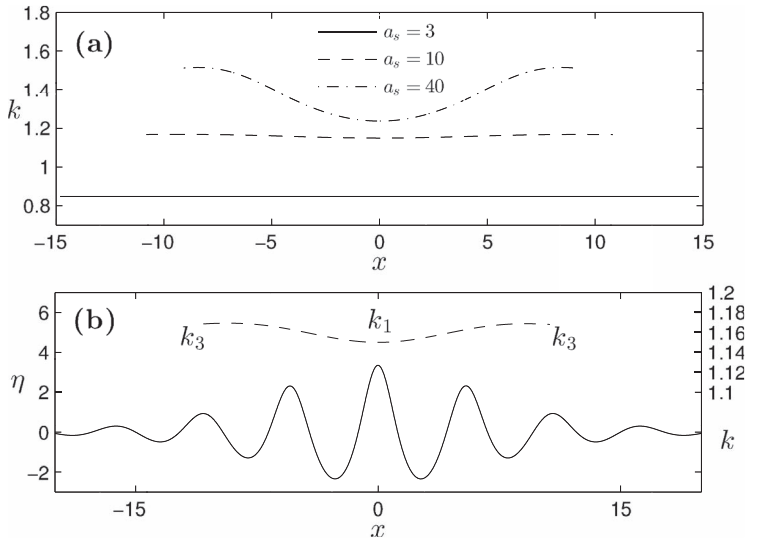

FIG. 11. (a) The packet local wavenumber k as a function of x. Only the x region between the largest peak denoted k_1 (when symmetrical) and third largest peak k_3 is shown. The decrease in x dependence of k with decreasing initial solitary wave amplitude supports the use of NLS theory in this regime. (b) The $a_s = 40$ packet (solid line) and its measured k (dashed-dotted line) plotted on the same x-axis to demonstrate the naming procedure for the local wavenumbers.

the maximum amplitude, discussed in more detail below. To obtain the local carrier wavenumber at any point in a packet, the instantaneous local wavelength $\lambda(x, t)$ was estimated as the current inter-peak distance at that point in the wavepacket at that time and then the time-mean of λ taken over the wave period. Fig. 11(a) gives examples of the calculated wavenumbers $k(x) = 2\pi/\lambda$ for the packets initialized from solitary waves with $a_s = 3$, 10, and 40. The region from the highest peak (when symmetrical), with local wavenumber denoted by k_1, to the third highest peak (with local wavenumber k_3) is shown, and the naming procedure for the local wavenumber is demonstrated in Fig. 11(b). Only the region from the highest peak to the third highest peak is shown, since, as can be seen in Fig. 11(a), the local wavenumber appears to approach a constant beyond the third peak. This held for all solutions, except the extended solutions where the determination of local wavenumber near the third peak became inaccurate. Therefore, k_1 gives a measure of the minimum k in the packet and k_3 gives an approximate measure of the maximum. The relation $k = 2\pi/\lambda$ is useful only for the near-linear packets of Sec. IV B 1 when the carrier waves are close to sinusoidal. When there are few crests inside the packet, as for the near-KdV packets of Sec. IV B 2 it is more useful to use the wavelength λ directly.

1. Strong rotation, small amplitude ($A \ll 1$), near-linear packets

Grimshaw and Helfrich[2] note the similarity in appearance of the small amplitude wavepackets (Fig. 9(a)) to the nonlinear Schrödinger bright soliton solution. Taking the wavenumber of the carrier wave to be k_c, Grimshaw and Helfrich[2] thus derive an extended, higher-order NLS for the Ostrovsky equation and present envelope soliton solutions of the equation. The carrier wave has "chirped" wavenumber equal to $3k_c/2$ due to nonlinearity, and the solution also predicts nonlinear corrections to both the linear phase and group velocities. The observation that the packet envelope is similar to the NLS soliton is also connected with the results here as it has been shown that from initial conditions such as localised hump perturbations to a uniform water wave[9] and non-uniform initial states in Bose-Einstein condensates,[10] stable solitons can form through MI. It is thus suggested that the nonlinear packet in the strong rotation, small amplitude regime could be a stable soliton formed from MI due to weak nonlinear effects in the slowly-varying near-linear wavetrain formed by the rapid dispersive destruction of the initial hump perturbation. Moreover, the observed wavenumbers in the computed packet solutions appear to lie sufficiently far from k_c to suggest the standard NLS

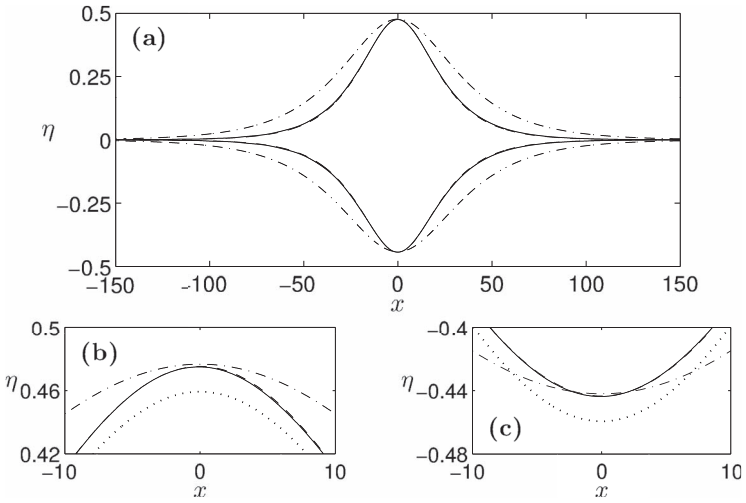

FIG. 12. (a) The envelope of the $a_s = 4$ converged packet (solid line), along with the envelope predictions from the standard NLS (dashed line) and higher-order NLS (dashed-dotted line), both with the A_2 correction. The standard NLS with A_2 correction is indistinguishable from the $a_s = 4$ converged packet. (b) and (c) Details of the extrema of the packet in (a) with the symmetrical standard NLS envelope prediction without the A_2 correction (dotted line) included. The A_2 correction accurately captures the asymmetry of the packet.

bright soliton as an accurate model. This section tests the accuracy of the standard NLS soliton in the strong rotation regime.

For $k > k_c$ (unstable) the standard NLS has bright soliton solution,

$$A = a\,\mathrm{sech}(KX)\exp(-\mathrm{i}\sigma t) \quad \text{where} \quad K = a\,(-\omega_2/\omega_{0kk})^{1/2}, \quad \sigma = \omega_2 a^2/2, \tag{27}$$

which corresponds in the original problem to the asymptotically correct solution,

$$\eta \approx 2a\,\mathrm{sech}[K(x - c_g t)]\cos[k(x - c_c t)] \quad a \ll 1, \tag{28}$$

where $c_c = (\omega_0 + \sigma)/k$ is the phase speed of the carrier wave. One shortcoming of solution (28) is its up-down symmetry as Fig. 10 suggests that an accurate model should display up-down asymmetry as found in the packets. The next term A_2 in expansion (8) has precisely the correct asymmetry and can be written[2] in the form $A_2 = \chi A^2$ where $\chi = 2k^2/(12k^4 + 3)$. Including this term gives in the original problem, correct to second-order in the amplitude, the solution

$$\eta \approx 2a\,\mathrm{sech}[K(x - c_g t)]\cos[k(x - c_c t)] + 2a^2\chi\,\mathrm{sech}^2[K(x - c_g t)]\cos[2k(x - c_c t)]. \tag{29}$$

Fig. 12 gives a detailed comparison of solutions (28) and (29) with the numerically determined packet for $a_s = 4$. The value of the carrier wavenumber is taken as $k = k_1$, which is effectively constant throughout the packet as shown by Fig. 11(a), and amplitude $a = (\max\{\eta(x,t)\} - \min\{\eta(x,t)\})/2$. Fig. 12(a) shows that (29) is graphically indistinguishable from the numerically determined packet. Fig. 12(a) also includes the higher-order NLS soliton from Ref. 2 (including its second-order correction) which appears to be a less accurate model of the packet for these parameters. Figs. 12(b) and 12(c) give details near the extrema of the packet, including the solution (28) and thus showing that the term A_2 not only captures the asymmetry but also significantly increases the accuracy of the solution.

To further test the asymptotic validity of the (28) and (29) solutions, the Ostrovsky equation was integrated numerically taking (28) and (29), with the parameters of Fig. 12, as initial conditions. Fig. 13 shows the mean squared deviation (MSD) from the initial condition, $\int[\eta(x,t) - \eta(x,0)]^2\,\mathrm{d}x$ measured when a crest is at the origin (x-symmetric), as a function of time. Although the standard NLS packet with A_2 correction appears indistinguishable from the numerical packet solution in Fig. 12, Fig. 13 shows the MSD converging to a deviation slightly less than 0.007. This constant deviation appears to arise from the absence in the NLS solution (29) of exponentially small "tails" (discussed in depth below) found in the converged packets. Fig. 13 also includes the MSD for the

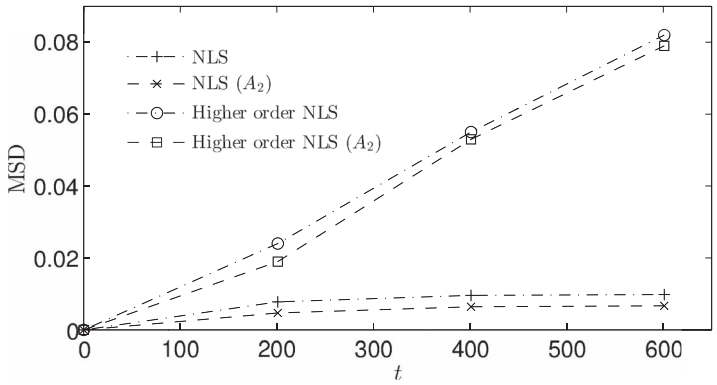

FIG. 13. The mean-squared-deviation (MSD) from the initial state for numerical integrations of the Ostrovsky equation with the standard and higher-order NLS solitons (with and without the A_2 correction) set as the initial conditions as a function of time, t. The parameters used are those for the NLS solitons for the $a_s = 4$ packet in Fig. 12.

higher-order NLS soliton of Fig. 12 which increases monotonically indicating perhaps that this higher-order NLS soliton with $k = k_c$ is not as close to an asymptotic solution of the Ostrovsky equation for these parameter values.

Fig. 14 shows the wavenumber estimate k_B from Sec. IV A with the k_1 and k_3 wavenumbers as a function of initial solitary wave amplitude a_s. The values of k_1 and k_3 from the numerical solutions are all greater than $k_c \approx 0.76$, thus satisfying the wavenumber criterion (7) for instability, and the agreement with k_B is reasonable. NLS theory predicts a constant k for a given a_s as shown by the coincidence of k_1 and k_3 up to $a_s \sim 10$, i.e., $\eta_{\max} \sim 3$ (see also Fig. 11(a)). For larger a_s (approaching the weak-rotation, near-KdV region) the wavenumber varies with x as these larger waves are too strongly nonlinear for the weakly-nonlinear NLS approximation to apply. The ends of the packet should merge with the linear theory and so it is to be expected that k_B would predict k_3 (closer to edge of the packet) more closely than k_1, and this is indeed seen in the solutions. Over the entire range of a_s here, k_B estimates k_3 to within 16%, lying always between k_3 and the higher-order NLS prediction[2] of $3k_c/2$. The small deviation of k_B from k_3 might be ascribable to the growth of nearby k once a band of wavenumbers is unstable, to inaccuracies in the two-phase stationary phase approximation for k near k_c, or to the approximations required to derive the criterion (25).

Figs. 15 and 16 show the phase velocity c_1 measured at the middle of the packet (the point associated with the wavenumber k_1) and the group velocity s of the numerical solutions, along with the velocity predictions $c_c(k_1)$, $c_g(k_1)$ (using the numerically determined k_1) from the soliton solution

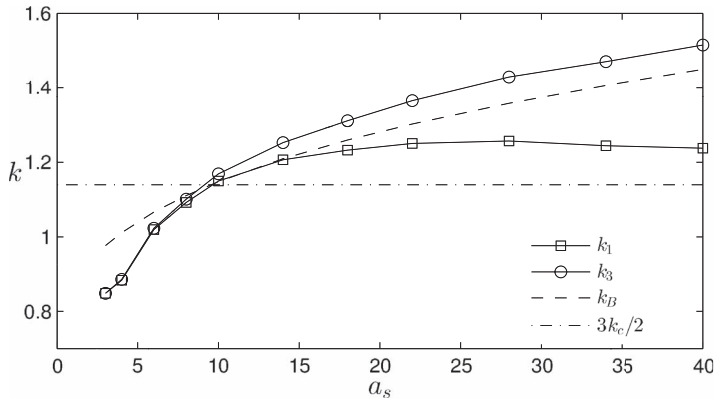

FIG. 14. The wavenumber predictions from modulation instability (k_B, dashed line), higher-order NLS ($3k_c/2$, dashed-dotted line), and numerical measurements k_1 (squares) and k_3 (circles).

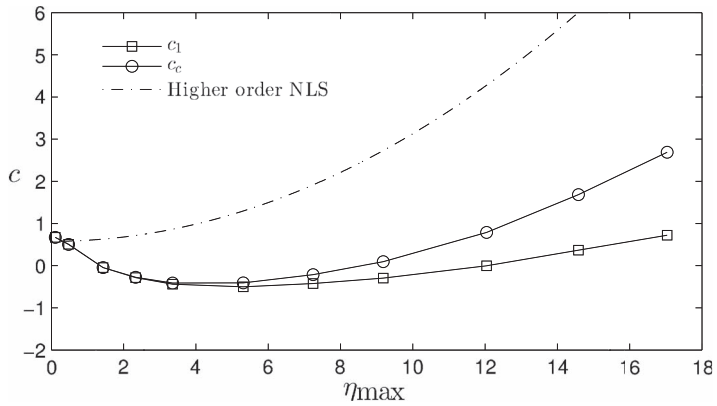

FIG. 15. Maximum phase velocity (middle of the packet) predictions, $c_c(k_1)$ (circles), and higher-order NLS (dashed-dotted line), along with the numerical measurements c_1 (squares). The agreement between c_1 and $c_c(k_1)$ is close for $\eta_{\max} \lesssim 5$.

(28) and (29) and the extended NLS. The predictions from the standard NLS soliton solution are indistinguishable from the numerically determined values in the small amplitude regime, $\eta_{\max} \lesssim 5$.

While the agreement of the numerics with the standard NLS theory is good, it should be noted that the observed wavenumbers of the smallest amplitude packets are close to k_c where the second-order dispersion term (ω_{0kk}) in the NLS is zero. As noted in Ref. 2, for sufficiently small ω_{0kk}, the effect of third-order dispersion $\omega_{0kkk} = \mathrm{d}^3\omega_0/\mathrm{d}k^3$ must be considered. The NLS for wave groups near the zero-dispersion point ($k = k_c$) can be written[2]

$$\mathrm{i}A_t + \tfrac{1}{2}\omega_{0kk}A_{XX} - \omega_2|A|^2A = \mathrm{i}\tfrac{1}{6}\omega_{0kkk}A_{XXX}, \tag{30}$$

where the term on the right-hand side gives the effect of third-order dispersion. To investigate the necessity of including the higher-order dispersion, the two dispersive terms are plotted alongside each other in Fig. 17 for two of the smallest converged packets ($a_s = 3, 6$). Fig. 17 shows that the second-order dispersion term dominates helping to explain why the properties of these packets are so well described by the standard NLS. However, third-order dispersion can be as much as 10% of second-order dispersion in places and so it is likely that it will have some effect. Because of the relative smallness of third-order dispersion it can be considered as a small perturbation in (30). For a NLS bright soliton this perturbation introduces exponentially small trailing oscillations[12] or "tails" and these are seen upon close examination of the small amplitude converged packets. It was to obtain an explicit soliton solution without radiative leakage that Grimshaw and Helfrich[2] followed the approach from nonlinear optics of including higher-order mixed nonlinear-dispersive terms in

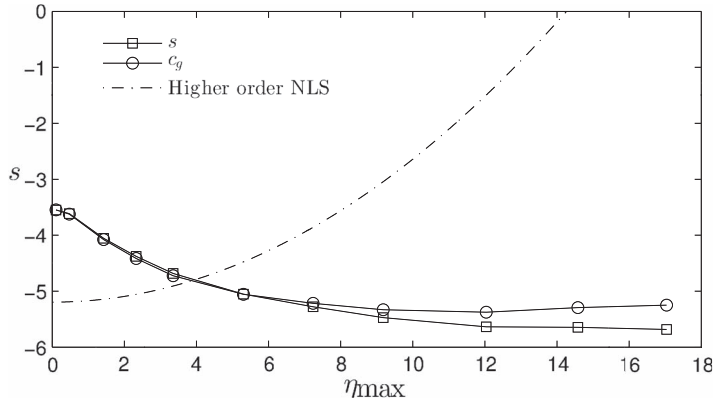

FIG. 16. Group velocity predictions, $c_g(k_1)$ (circles) and higher-order NLS (dashed-dotted line), along with numerical measurements s (squares). The agreement between s and $c_g(k_1)$ is close for $\eta_{\max} \lesssim 7$.

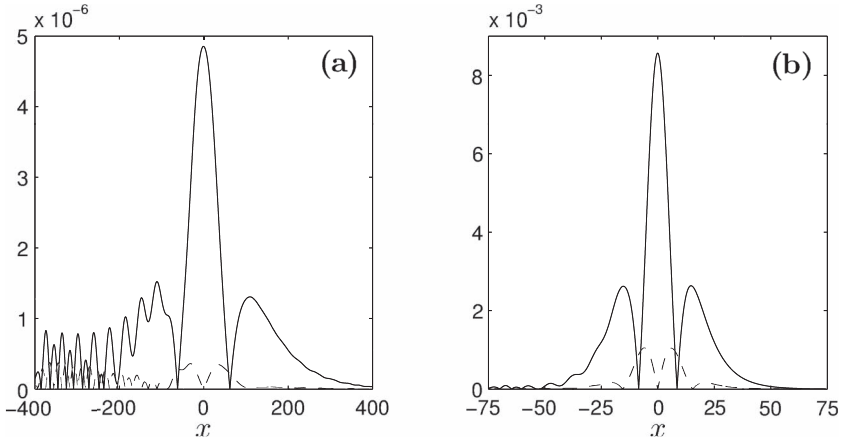

FIG. 17. The magnitudes of the second-order ($|\omega_{0kk}A_{XX}/2|$, solid line) and third-order ($|\omega_{0kkk}A_{XXX}/6|$, dashed line) linear dispersive terms of the NLS equation for the (a) $a_s = 3$ and (b) $a_s = 6$ converged packets. The oscillations on the left of the figures are caused by exponentially small tails.

their governing equation. However they note, as has been seen above, that these higher-order terms do not appear to improve agreement with the numerical solutions. Fig. 18 shows the packet half-amplitude, $|A|$, for the converged packets $a_s = 3$ and $a_s = 4$ plotted on a highly vertically expanded scale. The tails are clearly visible and are closely comparable to those in Fig. 2 of Ref. 12.

Wai, Chen, and Lee[12] derived predictions for the wavenumber and amplitude of the tails which were later refined by Grimshaw.[13] In order to compare the results here with those of Ref. 13, (30) is written in its canonical form using the scalings $T = t/|\omega_{0kk}|$, $A = |\omega_{0kk}/\omega_2|^{1/2}\phi$ and the transformations $\phi = \psi^*$, $X = -Y$ to give the equation

$$\mathrm{i}\psi_T + \tfrac{1}{2}\psi_{YY} + |\psi|^2\psi = \mathrm{i}\beta\psi_{YYY} \quad \text{with} \quad \beta = |\omega_{0kkk}/\omega_{0kk}|/6. \tag{31}$$

The wavenumber prediction $k \sim 1/(2\beta)$ from Ref. 13 gives, for the $a_s = 3$ and $a_s = 4$ packets, tail wavenumbers of 0.31 and 0.47, respectively, to be compared with the numerically determined values of 0.17 and 0.89. The corresponding tail amplitude predictions (in the transformed coordinates) are 10^{-13} and 10^{-5} to be compared with the measured values of 10^{-4} and 10^{-4}. Apart from the $a_s = 3$ tail amplitude, the predictions appear reasonable given the difficulty of measuring such small terms

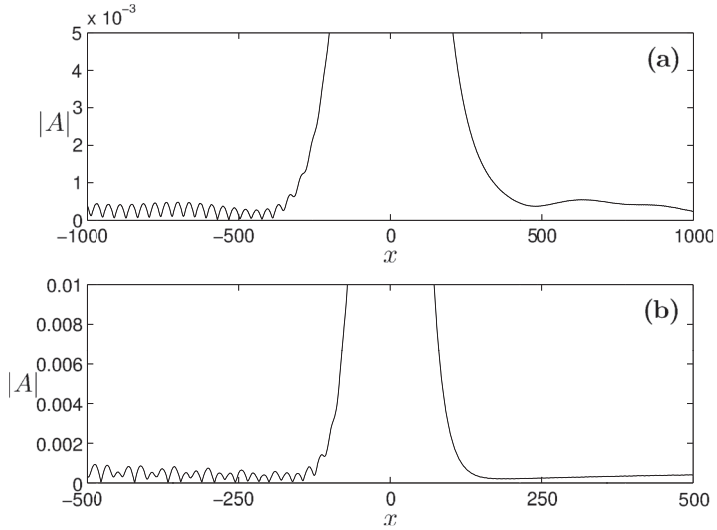

FIG. 18. The packet half-amplitude $|A|$ plotted on a highly vertically expanded scale for the (a) $a_s = 3$ and (b) $a_s = 4$ converged packets showing the oscillating tails caused by third-order dispersion.

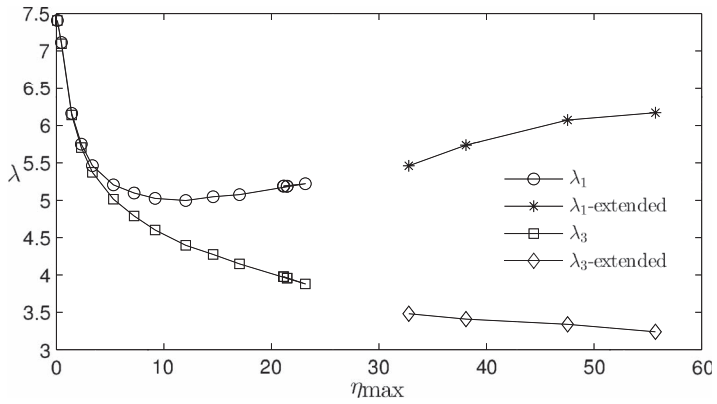

FIG. 19. Weak-rotation (large amplitude) packet wavelength measurements λ_1 (circles) and λ_3 (squares) for packets arising from KdV solitary wave decay and λ_1 (stars) and λ_3 (diamonds) from extended solutions. Note here λ_1 and λ_3 refer to the same positions in the wavepacket as k_1 and k_3, respectively (see Fig. 11(b)).

in an evolving flow, since here the envelope has been obtained from the full numerical solution of the Ostrovsky equation and, so includes the carrier wave, whereas the integrations in Ref. 12 are for the envelope equation (31) only.

2. Weak-rotation ($\epsilon = A^{-1} \ll 1$), near-KdV wavepackets

As noted in Sec. II, when the scaling in this region is chosen as the appropriate KdV scaling for η, x, and t, the governing equation transforms to (3) with coefficient $\epsilon^2 = A^{-2} \ll 1$ on the right-hand side, giving the small rotational perturbation to the KdV. This is precisely the equation considered by Gilman, Grimshaw, and Stepanyants[18] and the wavepackets in the weak-rotation regime here have many features in common with the solutions presented there. The weakness of rotational effects means that the initial KdV soliton persists for relatively long (KdV-scaled) times, decaying only slowly due to linear wave radiation.[2,14] By determining this linear radiation Grimshaw and Helfrich[2] predict that in this regime the wavepacket amplitude should oscillate with decaying amplitude about a fixed constant value as $a_s \to \infty$, precisely as seen in Fig. 10, where all initial conditions with $a_s \gtrsim 100$ evolve to the same limit packet (referred to as the KdV-IC-limit packet below) with $\eta_{\max} \sim 20$ and so $\epsilon \sim 0.05$. Grimshaw and Helfrich[2] point out that for sufficiently small initial conditions the model of a radiating KdV soliton is inappropriate as the radiated wavetrain cannot separate from the leading soliton. This corresponds to the strong-rotation, near-linear regime, described above, where the wavepacket appears to arise from MI in the dispersive wavetrain behind the leading disturbance. Converged higher amplitude, weaker rotation (and so smaller ϵ) extended wavepackets are obtained

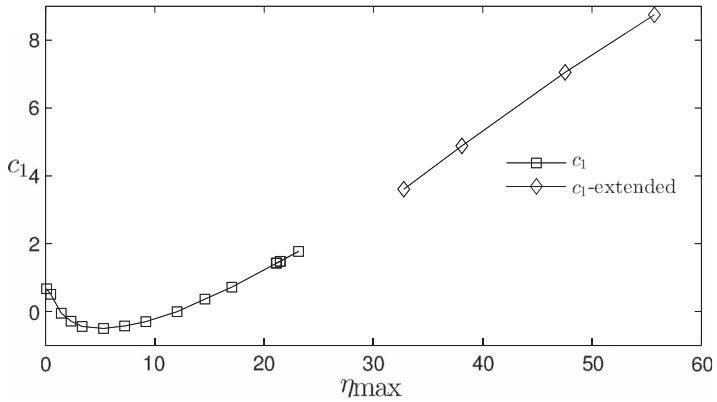

FIG. 20. Weak-rotation (large amplitude) maximum phase velocity (middle of the packet) measurements, c_1, of packets created from solitary wave decay (squares) and from extended solutions (diamonds).

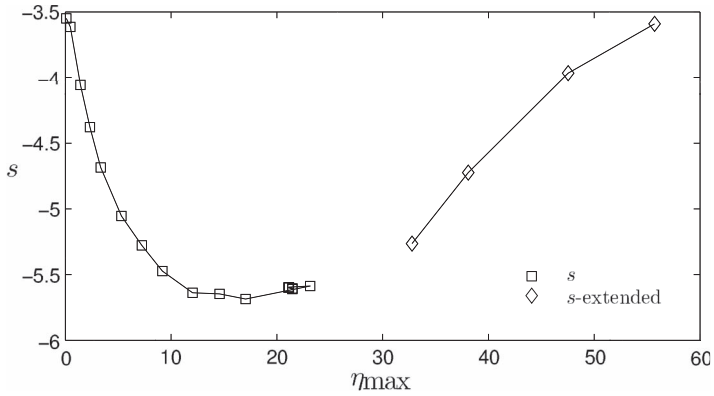

FIG. 21. Weak-rotation (large amplitude) group velocity measurements, s, of packets created from solitary wave decay (squares) and from extended solutions (diamonds).

from evolutions initialised with scaled converged packets from solitary wave decay. Figs. 19–21 show the computed wavelength, phase and group velocities for the higher amplitude solutions and extended solutions. Note that on each graph there are 5 entries for $\eta_{\max} \sim 20$ corresponding to the five integrations for $a_s \gtrsim 100$ which all evolve to the KdV-IC-limit packet.

The Ostrovsky equation has an exact parabolic solution[18] and a notable feature of the higher amplitude packets is that the lower envelope of the packet becomes increasingly close to parabolic with the packet solutions taking the appearance of a train of solitary waves propagating adiabatically[18] through a more slowly-varying background state of finite extent. Their dynamics is thus similar to that described in Ref. 18 where a single solitary wave is shown propagating adiabatically through an infinite periodic background. To quantify this observation a parabola

$$\eta = \alpha_2(\zeta - \zeta_0)^2 + \alpha_0 \quad \text{where} \quad \zeta = x - st, \tag{32}$$

was fitted by least squares to the bottom 40% of the lower envelope of the solutions. The values of α_2 for these weak-rotation solutions are shown in Fig. 22 and the parabolas for the KdV-IC-limit packet from $a_s = 400$ and the largest extended solution are shown in Figs. 23(a) and 23(b). The fit in both examples is good. The value of α_2 for the KdV-IC-limit packet from $a_s = 120$, 160,

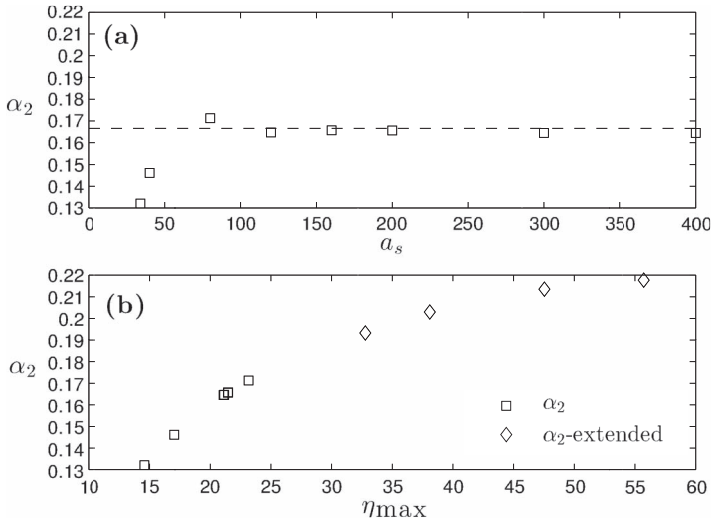

FIG. 22. The quadratic coefficient α_2, obtained from a least squares fit of a parabola to the lower envelope of the weak-rotation (large amplitude) wavepackets, as a function of (a) the initial solitary wave amplitude a_s, and (b) the maximum wave packet height $\eta_{\max}$. The dashed line represents the Ostrovsky parabola value, $\alpha_2 = 1/6$. The KdV-IC-limit packets formed from the decay of a solitary wave appear to have the same value of α_2 as the Ostrovsky parabola.

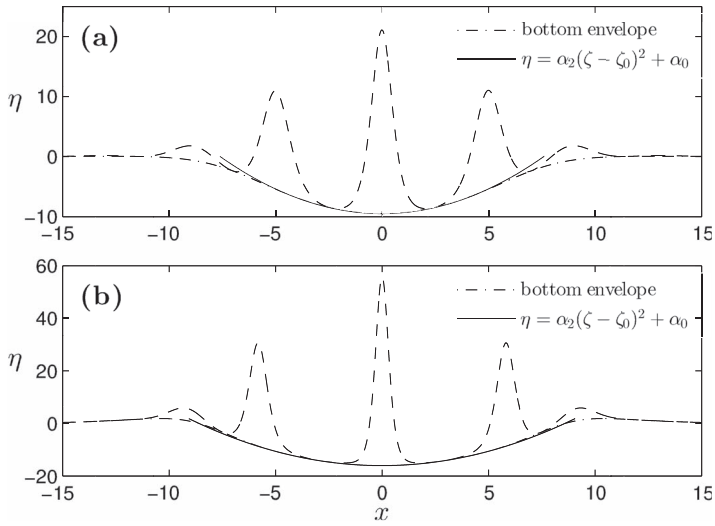

FIG. 23. Weak-rotation (large amplitude) packet solutions (dashed lines) for a solution created by solitary wave decay (a) the KdV-IC-limit packet from $a_s = 400$ and an extended solution (b), along with the fitted parabolas (solid lines) and the lower packet envelopes (dashed-dotted lines).

200, 300, and 400 coincides with the exact parabolic solution of the Ostrovsky equation for which $\alpha_2 = 1/6$ (Fig. 22(a)), but the velocity prediction from the Ostrovsky parabola of $s = -2\alpha_0$ ($\alpha_0 \sim -9.5$) differs in both direction and magnitude, from the packet envelope velocity. This appears to reflect an interaction between the solitons within the packet and the slowly-varying (when KdV-scaled) background. The parabolic fit for the extended packets is even closer (Fig. 23) but the values for α_2 exceed 1/6 (Fig. 22(b)). This might be related to their being inaccessible from single hump initial conditions. Similar to the small amplitude, strong rotation packets, all weak-rotation packets appeared to have tails. Fig. 24 shows the KdV-IC-limit packet ($a_s = 400$) on a vertically expanded scale. Unlike the tails in the near linear regime which show modulations in their amplitude, the tail amplitude here appears to be independent of x.

V. DISCUSSION

An accurate numerical method has been presented for determining wavepacket solutions of the Ostrovsky equation by requiring that the normalized mean-square-deviation (26) over one period in the co-moving frame is at most 10^{-5}. Using this method converged wavepacket solutions of the parameter-free Ostrovsky equation (3) have been obtained with amplitudes covering the range from $\eta_{\max} = 0.1$ to $\eta_{\max} = 40$. The precision of the method allows accurate measurement of the phase speed and local wavenumber for individual crests, and the shape and group speed of the packet envelopes. The envelopes can be divided conveniently into two regimes: a small amplitude, strong

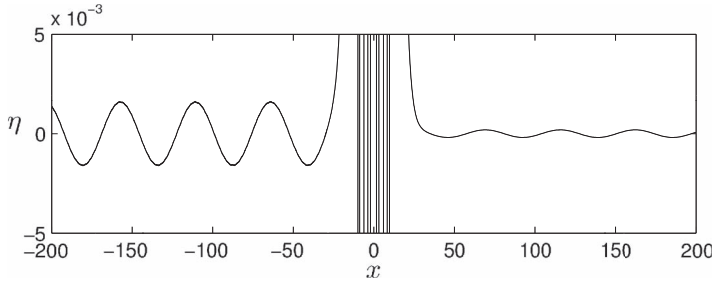

FIG. 24. A snapshot of the KdV-IC-limit packet ($a_s = 400$) packet showing a typical tail in the weak-rotation limit.

rotation, near linear regime, where the relevant small parameter is the wavepacket amplitude, and a weak-rotation, near KdV regime where the relevant small parameter, measuring the strength of the rotation, is the inverse of the amplitude of the packet in the parameter-free Ostrovsky equation.

In the near linear regime the computed wavenumber, k, of the carrier wave takes a unique constant value throughout each packet. This value of k gives immediately a unique linear group speed through the linear dispersion relation (5) and this speed coincides with the numerically determined group speed of the packets (Fig. 16). This leads to the hypothesis that the packets can be modelled as bright solitons of the NLS equation. With the carrier wavenumber k determined, the only free parameter in the expression for the NLS soliton (29) is the amplitude, $a = (\max\{\eta(x,t)\} - \min\{\eta(x,t)\})/2$. With a determined for each packet, the phase speed is given immediately through (27), a weakly-nonlinear correction to the linear dispersion relation, and once again this speed coincides with the numerically determined speed of crests within the packets (Fig. 15). The amplitude a and wavenumber k uniquely determine the packet shape through (29) and, in particular, its asymmetry due to second-order (in a) terms is given immediately. These packet shapes closely model the numerically determined wavepackets (Fig. 12). The accuracy of this NLS packet is confirmed by taking the packet as the initial condition in the Ostrovsky equation and demonstrating that the solution deviates little from the initial condition during the evolution (Fig. 13).

Grimshaw and Helfrich[2] point out that the wavenumbers of the packets can be expected to be near $k = k_c$, the wavenumber corresponding to the maximum of the group velocity. Precisely at $k = k_c$ the second-order dispersion of the usual NLS equation vanishes and third-order dispersion dominates and thus Grimshaw and Helfrich[2] derive a higher-order NLS equation which incorporates the effects of both second and third-order dispersion. A model[2] of the packets obtained by setting $k = k_c$ in this higher-order NLS equation seems less successful in its predictions than the standard NLS soliton (29). This is perhaps explained by Fig. 17 which shows that, throughout the numerically determined wavepackets, second-order dispersion is approximately 10 times larger than third-order dispersion. Third-order dispersion can thus be treated as a small perturbation to the soliton (29), following Grimshaw,[13] leading to a prediction of exponentially small tails which are indeed observed (Fig. 18) and closely resemble those in Fig. 2 of Wai, Chen, and Lee.[12]

Modulational instability generates solitons from initial hump perturbations in water waves[9] and Bose-Einstein condensates[10] and thus is suggested as a possible mechanism for the wavepackets observed in the strong rotation, near linear regime here. Standard results are applied by noting that any initial disturbance rapidly disperses into a linear wavetrain with slowly varying local wavenumber and amplitude. Over much longer times weakly nonlinear effects allow MI of this wavetrain and a local instability criterion (25), which must be satisfied in addition to the carrier wavenumber condition (7), is suggested. The MI growth rate increases as k increases above k_c, whereas linear arguments here and previously[2] suggest that disturbance energy disperses slowest near $k = k_c$. Criterion (25) captures the competition between these two effects, predicting the position and time when a nonlinear packet should first appear and an estimate of the carrier wavenumber for the packet, all of which are in accord with the numerically determined values (Fig. 14).

In the weak-rotation limit the initial KdV soliton does not disperse rapidly but persists for relatively long (KdV-scaled) times, decaying only slowly due to linear wave radiation.[2,14] Sufficiently large initial solitons (sufficiently weak rotation, $a_s \gtrsim 100$) all evolve to the same KdV-IC-limit packet of Fig. 23(a) as predicted by Grimshaw and Helfrich[2] by considering the weak radiated linear wavefield. The wavepackets are shown to resemble a wavetrain of KdV solitons propagating adiabatically through a slowly varying (KdV-scaled) parabolic background of finite extent, with dynamics exactly those of the single KdV soliton on the infinite periodic background of Gilman, Grimshaw, and Stepanyants.[18] These wave packets also appear to possess exponentially small tails. The analytical questions raised by the observations are under investigation.

ACKNOWLEDGMENTS

The authors are grateful to two anonymous referees whose questions and comments led to a clearer exposition. A.J.W. was supported by UCL Mathematics Department under the Wren Bequest and Sir James Lighthill Scholarships.

[1] K. R. Helfrich, "Decay and return of internal solitary waves with rotation," Phys. Fluids **19**, 026601 (2007).
[2] R. H. J. Grimshaw and K. R. Helfrich, "Long-time solutions of the Ostrovsky equation," Stud. Appl. Math. **121**, 71–88 (2008).
[3] M. Stastna, F. J. Poulin, K. L. Rowe, and C. Subich, "On fully nonlinear, vertically trapped wave packets in a stratified fluid on the f-plane," Phys. Fluids **21**, 106604 (2009).
[4] K. R. Khusnutdinova and K. R. Moore, "Initial-value problem for coupled Boussinesq equations and a hierarchy of Ostrovsky equations," Wave Motion **48**, 738–752 (2011).
[5] R. H. J. Grimshaw, K. R. Helfrich, and E. R. Johnson, "Experimental study of the effect of rotation on nonlinear internal waves," Phys. Fluids **25**, 056602 (2013).
[6] D. Farmer, Q. Li, and J.-H. Park, "Internal wave observations in the South China Sea: The role of rotation and non-linearity," Atmos.-Ocean **47**, 267–280 (2009).
[7] Q. Li and D. M. Farmer, "The generation and evolution of nonlinear internal waves in the deep basin of the South China Sea," J. Phys. Oceanogr. **41**, 1345–1363 (2011).
[8] V. Vlasenko, J. C. Sanchez Garrido, N. Stashchuk, J. Garcia Lafuente, and M. Losada, "Three-dimensional evolution of large-amplitude internal waves in the Strait of Gibraltar," J. Phys. Oceanogr. **39**, 2230–2246 (2009).
[9] V. I. Shrira and V. Geogjaev, "What makes the Peregrine soliton so special as a prototype of freak waves?" . Eng. Math. **67**, 11–22 (2010).
[10] L. D. Carr and J. Brand, "Spontaneous soliton formation and modulational instability in Bose-Einstein condensates," Phys. Rev. Lett. **92**, 040401 (2004).
[11] R. H. J. Grimshaw, D. Pelinovsky, E. Pelinovsky, and T. Talipova, "Wave group dynamics in weakly nonlinear long-wave models," Phys. D **159**, 35–57 (2001).
[12] P. Wai, H. Chen, and Y. Lee, "Radiations by "solitons" at the zero group-dispersion wavelength of single-mode optical fibers," Phys. Rev. A **41**, 426 (1990).
[13] R. Grimshaw, "Weakly nonlocal solitary waves in a singularly perturbed nonlinear Schrodinger equation," Stud. Appl. Math. **94**, 257–270 (1995).
[14] R. H. J. Grimshaw, J.-M. He, and L. A. Ostrovsky, "Terminal damping of a solitary wave due to radiation in rotational systems," Stud. Appl. Math. **101**, 197–210 (1998).
[15] M. J. Ablowitz and H. Segur, *Solitons and the Inverse Scattering Transform*, Studies in Applied Mathematics Series (Society for Industrial and Applied Mathematics, 2006).
[16] R. H. J. Grimshaw and K. R. Helfrich, "The effect of rotation on internal solitary waves," IMA J. Appl. Math. **77**, 326–339 (2012).
[17] M. Stastna and K. Rowe, "On weakly nonlinear descriptions of nonlinear internal gravity waves in a rotating reference frame," Atl. Electron. Math. **2**, 30 (2007).
[18] O. A. Gilman, R. H. J. Grimshaw, and Y. A. Stepanyants, "Dynamics of internal solitary waves in a rotating fluid," Dyn. Atmos. Oceans **23**, 403–411 (1996).
[19] M. J. Lighthill, "Contributions to the theory of waves in non-linear dispersive systems," IMA J. Appl. Math. **1**, 269–306 (1965).
[20] H. Hasimoto and H. Ono, "Nonlinear modulation of gravity waves," J. Phys. Soc. Jpn. **33**, 805–811 (1972).
[21] T. B. Benjamin and J. E. Feir, "The disintegration of wave trains on deep water," J. Fluid Mech. **27**, 417–430 (1967).
[22] A. M. Kamchatnov, *Nonlinear Periodic Waves and Their Modulations: An Introductory Course* (World Scientific Publishing Company, Incorporated, 2000), p. 305.
[23] L. N. Trefethen, *Spectral Methods in MATLAB*, Vol. 10 (Society for Industrial and Applied Mathematics, 2000), p. 111.
[24] J. R. Cash and A. H. Karp, "A variable order Runge-Kutta method for initial value problems with rapidly varying right-hand sides," ACM Trans. Math. Software (TOMS) **16**, 201–222 (1990).
[25] S. A. Orszag and C. M. Bender, *Advanced Mathematical Methods for Scientists and Engineers* (McGraw Hill, New York, 1978), p. 276.